Energy Budget Constraints on the Time History of Aerosol Forcing and Climate Sensitivity

C. J. Smith[1,2], G. Harris[3], M. D. Palmer[3], N. Bellouin[4], G. Myhre[5], M. Schulz[6], J.-C. Golaz[7], M. Ringer[3], T. Storelvmo[8] and P. M. Forster[1]

[1]Priestley International Centre for Climate, University of Leeds, UK.

[2]International Institute for Applied Systems Analysis (IIASA), Laxenburg, Austria.

[3]Met Office Hadley Centre, Exeter, UK.

[4]Department of Meteorology, University of Reading, UK.

[5]Center for International Climate and Environmental Research in Oslo (CICERO), Norway.

[6]Norwegian Meteorological Institute, Oslo, Norway.

[7]Lawrence Livermore National Laboratory, Livermore, CA, USA.

[8]Department of Geosciences, University of Oslo, Norway.

Corresponding author: Chris Smith (c.j.smith1@leeds.ac.uk)

Key Points:

- We determine the most plausible time history of aerosol forcing that matches surface temperature and Earth energy uptake constraints
- Constrained aerosol forcing is relatively constant between 1972 and 2014, unlike in some climate models that show an increasing forcing
- The best estimate aerosol forcing using this method is -1.12 W m^{-2} for 2005-14 relative to 1750.

Abstract

An observationally-constrained time series of historical aerosol effective radiative forcing (ERF) from 1750 to 2019 is developed in this paper. We find that the time history of aerosol ERFs diagnosed in CMIP6 models exhibits considerable variation and explore how the time history of aerosol forcing influences the probability distributions of present-day aerosol forcing and emergent metrics such as climate sensitivity. Using a simple energy balance model, trained on CMIP6 climate models and constrained by observed near-surface warming and ocean heat uptake, we derive estimates for the historical aerosol forcing. We find 2005-2014 mean aerosol ERF to be -1.1 (-1.7 to -0.5) W m^{-2} relative to 1750. Assuming an SSP2-4.5 forcing pathway, aerosol ERF in 2019 is -0.9 (-1.5 to -0.4) W m^{-2}. There is no strong trend in aerosol forcing between 1972 and 2014. This analysis also gives a 5-95% range of equilibrium climate sensitivity (ECS) of 1.9-6.0°C (best estimate 3.1°C) with a transient climate response (TCR) of 1.3-2.7°C (best estimate 1.8°C). We find TCR is not sensitive to the historical aerosol forcing time series used for constraint, although the upper bound of ECS is difficult to constrain this way.

Plain Language Summary

There are two main human drivers of climate change: (i) Greenhouse gas emissions, which warm the planet; and (ii) air pollution (aerosols) that offset some of this warming. Unfortunately, disentangling the effects of historical aerosol cooling is difficult based on the available observations. Therefore, we often use climate models to estimate how much aerosols have cooled the Earth since the start of the Industrial Revolution. Over some periods of the 20th Century, some climate models simulate less warming than has been observed since 1850. This may be because aerosol cooling in some climate models is too strong. Our approach combines the relationships between aerosol emissions and their cooling effects on temperature from 10 climate models with simpler representations of the underlying physics. This simpler mathematical framework allows us to more fully account for uncertainty in both the aerosol cooling and its effects on surface temperature and ocean heat uptake by running a much larger set of simulations. Our results suggest that the effect of aerosol cooling has been relatively constant from 1972 to 2014, and that some climate models do produce a stronger cooling in this time than is supported by the observations.

1 Introduction

Aerosol effective radiative forcing remains one of the most uncertain components of the present-day climate (Bellouin, Quaas, et al., 2020). Uncertainty in present-day forcing reduces our ability to confidently predict the future climate response to emissions (Forster et al., 2013) and the level of historical greenhouse gas warming masked by the cooling effect of aerosols (Samset et al., 2018). Aerosol forcing is the largest uncertainty governing future committed warming (Matthews & Zickfeld, 2012; Smith et al., 2019) and remaining carbon budgets consistent with Paris Agreement targets (Mengis & Matthews, 2020). In most future socio-economic scenarios, aerosol forcing is projected to become less negative over the 21st century (Gidden et al., 2019; Huppmann et al., 2018; Rogelj et al., 2018), promoting an increase in the rate of warming unless there is a concurrent reduction in greenhouse gas emissions (Shindell & Smith, 2019). The time history of aerosol ERF is a necessary input to many reduced-complexity climate models (Nicholls et al., 2020), which in turn may be driven by simple emissions-to-

forcing based relationships; these simple models find enormous utility when coupled to integrated assessment models (Huppmann et al., 2018).

Given its large uncertainty, aerosol forcing has remained an active research area. Several studies have quantified the aerosol effective radiative forcing (ERF) in the present day relative to pre-industrial based on observations, models, energy balance arguments, or a combination of approaches (Andrews & Forster, 2020; Bellouin, Quaas, et al., 2020; Boucher et al., 2013; Fiedler et al., 2019; Forest, 2018; Forest et al., 2002, 2006; Myhre, Shindell, et al., 2013; Skeie et al., 2018; Smith et al., 2020; Zelinka et al., 2014). Fewer studies have attempted to diagnose a time series of aerosol forcing since 1750 or 1850 e.g. (Murphy et al., 2009; Prather et al., 2013; Shindell et al., 2013; Skeie et al., 2011)).

Our goal is define an aerosol ERF time series from 1750 to 2019 that is consistent with energy balance constraints from observations. Under the Radiative Forcing (RFMIP) and Aerosol Chemistry (AerChemMIP) Model Intercomparison Projects, aerosol forcing could be diagnosed directly from CMIP6 models. However, in the multi-model mean, CMIP6 model simulations of global-mean surface air temperature (GSAT) are cooler than observations throughout the latter part of the 20th Century before recovering to near-present levels of warming today (Flynn & Mauritsen, 2020). One hypothesis is that aerosol forcing in the 20th Century may be too strong in some CMIP6 models, coupled with high transient climate response (TCR) that causes implausibly rapid recent warming in many models (Tokarska et al., 2020). Nevertheless, CMIP6 models remain an important line of evidence in determining historical aerosol forcing. Unlike for greenhouse gases, proxy records for aerosol forcing are sparse before widespread surface radiation measurements became available in the 1950s (Bellouin, Quaas, et al., 2020; Moseid et al., 2020). No global observations of aerosols were available until the satellite era (late 1970s), whereas CMIP6 models produce aerosol forcing estimates from 1850. Therefore, we use CMIP6 model forcing over the industrial era to inform our estimates of historical aerosol ERF, and "correct" for these responses by constraining the forcing estimates to observations of GSAT and Earth energy uptake (EEU).

2 Methods and Data

This section describes how the historical ERF time series are generated and how observational constraints are used with a simple energy-balance climate model to produce a best estimate and range of historical aerosol forcing estimates. A number of historical aerosol forcing time series are investigated. The primary focus of this study is an ensemble of time series generated from a simple relationship of global annual emissions to global annual historical aerosol ERF, using the CMIP6 aerosol emissions time series and tuning this relationship (which we call a "forcing emulator") on CMIP6 models where historical aerosol forcing estimates exist. Following the observational constraining we refer to this time series as "CMIP6-constrained". We also investigate replacing the CMIP6 emissions time series in the forcing emulator with a more recent global emissions inventory (ECLIPSE v6b (Stohl et al., 2015), referred to as "ECLIPSE-constrained"), and using scaled estimates of historical aerosol forcing from 10 CMIP6 models and one chemistry-transport model. This provides a total of 13 different historical aerosol forcing scenarios.

Throughout this paper, a probabilistic approach is taken, sampling 25,000 historical forcing timeseries per scenario with the same number of simple climate model configurations.

Uncertainties in the non-aerosol components of historical forcing (e.g. greenhouse gases and natural forcings) are also taken into account. The resulting GSAT and EEU time series from each ensemble member is compared to the observational constraints and a weighted posterior distribution produced of historical aerosol ERF.

2.1 Aerosol effective radiative forcing timeseries

2.1.1 CMIP6 model output

We start with 1850 to 2014 transient aerosol ERF derived from 10 GCMs (Fig. 1; Table 1). Seven models were provided under RFMIP (Pincus et al., 2016), two under AerChemMIP (Collins et al., 2017) and one used a similar method to AerChemMIP but with Atmospheric Model Intercomparison Project (AMIP) sea-surface temperatures (SSTs) rather than model-diagnosed SSTs (Golaz et al., 2019).

In the RFMIP models, aerosol ERF is diagnosed by running a transient climate integration with pre-industrial climatologies of sea-surface temperatures, sea-ice distributions and transient aerosol emissions for 1850 to 2014 or 2100 under SSP2-4.5 (piClim-histaer) and taking the top-of-atmosphere shortwave and longwave flux differences with respect to a 30-year atmosphere-only control run (piClim-control; Forster et al. (2016)). All non-aerosol forcings are set to 1850 levels, and only the aerosol precursor emissions are allowed to evolve, following the historical inventories from the Community Emissions Data System (CEDS; Hoesly et al. (2018)) and the historic global biomass burning emissions for CMIP6 (BB4CMIP; van Marle et al. (2017)). From AerChemMIP models we use parallel runs of historical SSTs with all historical forcings (histSST) and historical SSTs with all historical forcings except aerosol forcings set to pre-industrial levels (histSST-piAer). E3SM also followed this method (described in Golaz et al. (2019)).

Figure 1 shows the aerosol effective radiative forcing with respect to 1850 from CMIP6 models. Most models show a peak in negative aerosol forcing at some point between 1975 and 2010 before recovering in recent years, with MIROC6 an exception in which the peak does not occur until the end of the SSP historical period (2014).

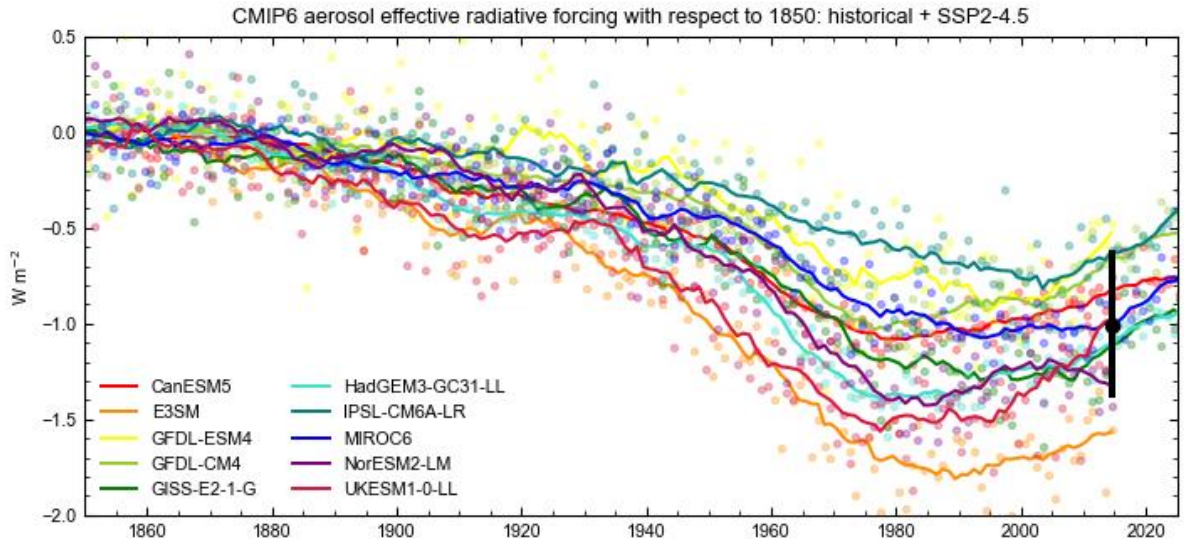

Figure 1: CMIP6 diagnosed net aerosol effective radiative forcing relative to 1850. Individual years are shown in dots with an 11-year Savitzky-Golay smoothing filter applied to show solid line. The black point and line represents the 17-model mean and range from Smith et al. (2020) for 1850-2014, which did not include E3SM.

Table 1: CMIP6 models providing transient historical aerosol ERF estimates. Runs extended beyond 2014 in RFMIP experiments followed an SSP2-4.5 forcing pathway. The HadGEM3-GC3.1 and IPSL-CM6A-LR models are currently unpublished on the Earth System Grid and considered preliminary.

Model	Long name	Modelling protocol	Ensemble members	Time period	References
CanESM5	Canadian Earth System Model, verison 5.0.3	RFMIP	3	1850-2100	Swart et al. (2019)
E3SM	U.S. Department of Energy (DOE) Energy Exascale Earth System Model (E3SMv1)	AMIP and AMIP with pre-industrial aerosols	3	1870-2014	Golaz et al. (2019)
GFDL-ESM4	Geophysical Fluid Dynamics Laboratory ESM4.1	AerChemMIP	1	1850-2014	
GFDL-CM4	Geophysical Fluid Dynamics Laboratory CM4.0	RFMIP	2	1850-2100	Held et al. (2019)
GISS-E2-1-G	Goddard Institute for Space Studies ModelE 2.1-G	RFMIP	1	1850-2100	Kelley et al., (submitted)
HadGEM3-GC31-LL	Met Office Hadley Centre Global Coupled Model 3.1	RFMIP (pre-ESGF version)	3	1850-2100	Williams et al. (2018)
IPSL-CM6A-LR	Institut Pierre Simon Laplace Climate Model 6A (low resolution)	RFMIP (pre-ESGF version)	1	1850-2100	Boucher et al. (submitted)
MIROC6	Model for Interdisciplinary Research on Climate, version 6	RFMIP	3	1850-2100	Tatebe et al. (2019)
NorESM2-LM	Norwegian Earth System Model, version 2	RFMIP	3	1850-2014	Seland et al. (2020)
UKESM1-0-LL	UK Earth System Model	AerChemMIP	1	1850-2014	Sellar et al. (2019)

151 2.1.2 Separation of aerosol components

152 For each CMIP6 model, the shortwave (SW) aerosol-radiation and aerosol-cloud
153 interaction components of the ERF ($ERFari_{SW}$ and $ERFaci_{SW}$) are determined using the
154 Approximate Partial Radiative Perturbation (APRP) method (Taylor et al., 2007; Zelinka et al.,
155 2014). The LW ERF from aerosol-cloud interactions ($ERFaci_{LW}$) was determined using the
156 difference between all-sky and clear-sky forcing (difference in cloud radiative effect) with the
157 LW ERF from aerosol-radiation interactions ($ERFari_{LW}$) estimated as the difference between
158 ERF_{LW} and $ERFaci_{LW}$. The APRP is not exact and a small residual term arises that varies over
159 time and by model (Fig. S1), some of which is related to a small surface albedo adjustment
160 (Ghan, 2013), but only the time-varying shapes and relative magnitudes of ERFari and ERFaci to
161 each other are important for this decomposition.
162
163 For the RFMIP models we calculate the APRP using the difference of each year of the
164 piClim-histaer run against every year of the piClim-control run before averaging across the 30
165 piClim-control years to determine the ERFari and ERFaci from each year of 1850 to 2100. This
166 method removes some non-linearities in the APRP (particularly in relation to the cloud fraction
167 adjustment part of ERFaci) alongside minimising the influence of internal variability. For the
168 AerChemMIP models and E3SM, APRP was calculated using the parallel all-forcing and 1850-
169 aerosol forcing AMIP ensemble members and averaged. In all cases where modelling groups
170 provided more than one ensemble member, the APRP decomposition is calculated separately in
171 each ensemble member and then averaged.

172 2.1.3 Forcing emulator

173 Simple emissions-based relationships are then fit to the APRP-derived ERFari and
174 ERFaci in each CMIP6 model:
175
176 $$ERFari = \alpha_{SO2} E_{SO2} + \alpha_{BC} E_{BC} + \alpha_{OC} E_{OC} \quad (1)$$
177 $$ERFaci = \beta \log(1 + E_{SO2}/s_{SO2} + (E_{BC+OC}/s_{BC+OC})) \quad (2)$$
178
179 In eqs. (1) and (2), E_{SO2}, E_{BC} and E_{OC} refer to emissions in Tg yr^{-1} of SO_2, black carbon
180 (BC) and organic carbon (OC), and α_{SO2}, α_{BC}, α_{OC}, β, s_{SO2} and s_{BC+OC} are scaling coefficients.
181 α values can be interpreted as the radiative efficiency of emission of each aerosol precursor
182 species.
183
184 Equation (1) follows from studies showing that ERFari scales linearly with emissions
185 (Johnson et al., 2019; Lund et al., 2018; Mahajan et al., 2013; Rap et al., 2013). Equation (2) is
186 an extension of the simple relationship of Stevens (2015) and is based on the understanding that
187 the change in cloud albedo is logarithmic with sulfate burden, and that burden scales with
188 emissions (Carslaw et al., 2013; Charlson et al., 1992). Including carbonaceous aerosol in eq. (2)
189 represented by the sum of BC and OC emissions is useful as some CMIP6 models include the
190 effects of BC and/or OC on the change in cloud condensation nuclei. The resulting forcing can
191 be substantial, for example a negative ERFaci to BC emissions in the MIROC6 model (Thornhill
192 et al., 2020). Equation (2) is found to give a good heuristic approximation of global-mean
193 ERFaci to a more sophisticated aerosol indirect effect model (Ghan et al., 2013) as shown in
194 Smith, Forster, et al. (2018).
195

196 α_{SO2}, α_{BC}, α_{OC}, β, s_{SO2} and s_{BC+OC} parameters in eqs. (1) and (2) are estimated using a
197 least-squares curve fit of each CMIP6 model's ERFari and ERFaci (Table 2). The multi-model
198 mean α coefficients (-2.4, +32.2 and -9.4 mW m^{-2} (Tg yr^{-1})$^{-1}$ for SO_2, BC and OC respectively)
199 are of similar magnitudes to the radiative efficiencies from Aerocom models (Myhre, Samset, et
200 al., 2013) for SO_2 and BC, and a little stronger for OC here. We do not attribute a nitrate forcing
201 to avoid overfitting and because not all models include the effects of nitrogen compounds on
202 aerosol formation. The best-fit values for s_{SO2} and s_{BC+OC} span several orders of magnitude. We
203 treat these terms as shape parameters, describing how linear or logarithmic the change in ERFaci
204 is with increasing anthropogenic SO_2 and carbonaceous aerosol emissions. The degree of
205 logarithmic behaviour that ERFaci exhibits to emissions differs considerably between GCMs
206 (Wilcox et al., 2015) and the possibility that ERFaci may be linear with emissions in some
207 CMIP5 models was discussed in Booth et al. (2018).
208
209
210 **Table 2:** Forcing emulator coefficients corresponding to eqs. (1) and (2) for each model and the
211 emulation of the multi-model mean forcing. For ERFaci the natural logarithms of s_{SO2} and
212 s_{BC+OC} in each model are used to inform the distributions of aerosol forcing.

	ERFari (mW m^{-2} (Tg yr^{-1})$^{-1}$)			**ERFaci**		
Model	α_{SO2}	α_{BC}	α_{OC}	β (W m^{-2})	s_{SO2} ($TgSO_2$ yr^{-1})	s_{BC+OC} (TgC yr^{-1})
CanESM5	-2.5	32.6	-0.4	0.727	58.9	24.6
E3SM	-0.9	24.8	-12.6	2.760	134.1	105.9
GFDL-CM4	-2.6	26.9	-2.1	3.494	691.8	382.0
GFDL-ESM4	-2.6	102	-3.0	1702	502 700	111 400
GISS-E2-1-G	-6.7	146	-44.1	0.562	117.8	16.0
HadGEM3-GC31-LL	-2.9	2.0	4.2	0.963	88.5	72.6
IPSL-CM6A-LR	-0.7	-56.1	8.8	1.096	358.3	518.2
MIROC6	-1.8	38.6	-14.2	0.773	117.2	35.0
NorESM2-LM	-1.3	3.0	-3.4	6746	1 024 000	547 900
UKESM1-0-LL	-2.4	2.6	0.0	0.741	39.6	227.9
Multi-model mean emulation	-2.4	32.2	-9.4	1.111	138.4	66.0

213
214
215 Figure 2 shows the emulated fits to each CMIP6 model from eqs. (1) and (2) as coloured
216 curves with the APRP-derived forcing from the GCMs in grey using an 1850 reference. It can be
217 seen that these emulated relationships give a good representation of each component of the
218 aerosol forcing in each model. We extrapolate these CMIP6 emulations back to 1750 in each
219 model, resulting in a small positive forcing in 1750. Where models do not provide an SSP2-4.5
220 future projection, we also extend these time series forward using eqs. (1) and (2). Finally, we re-
221 base all emulated time series to a 1750 reference (fig. 3), where the impacts of the different
222 shapes for historical aerosol forcing due to different parameter combinations are more clearly
223 seen. One notable feature in all time series is an increased forcing between 2014 and 2015 in the
224 emulated curves owing to a 16% reduction in global SO_2 emissions from the historical to SSP2-
225 4.5 datasets over one year.

226

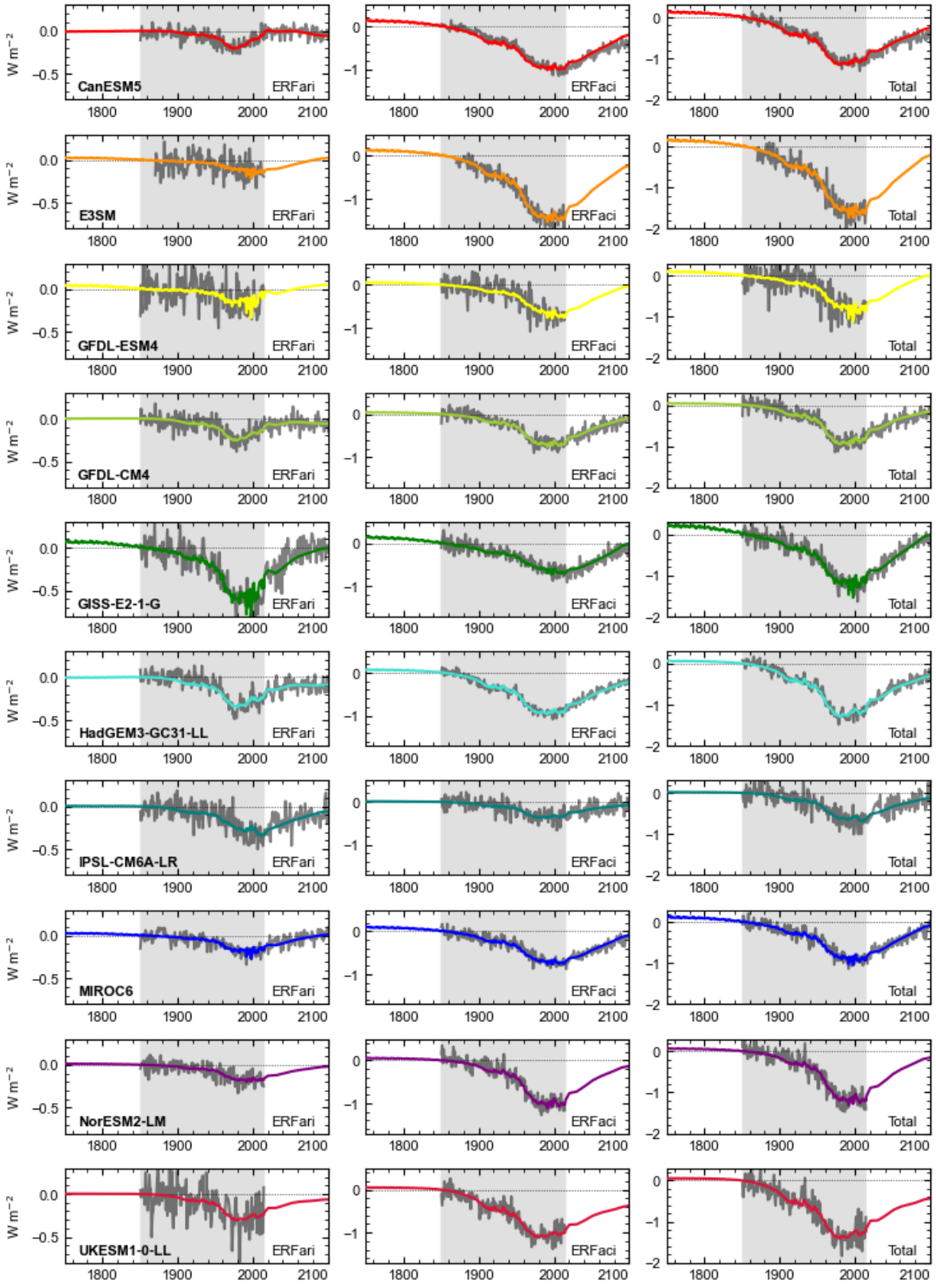
CanESM5
E3SM
GFDL-ESM4
GFDL-CM4
GISS-E2-1-G
HadGEM3-GC31-LL
IPSL-CM6A-LR
MIROC6
NorESM2-LM
UKESM1-0-LL
ERFari
ERFaci
Total
W m⁻²
1800
1900
2000
2100

227

Figure 2: simple emissions-based fits from eqs. (1) and (2) to ERFari (left), ERFaci (centre) and total aerosol forcing (right) for 10 CMIP6 models. Grey curves show the relevant forcing components from each GCM diagnosed using the APRP method.

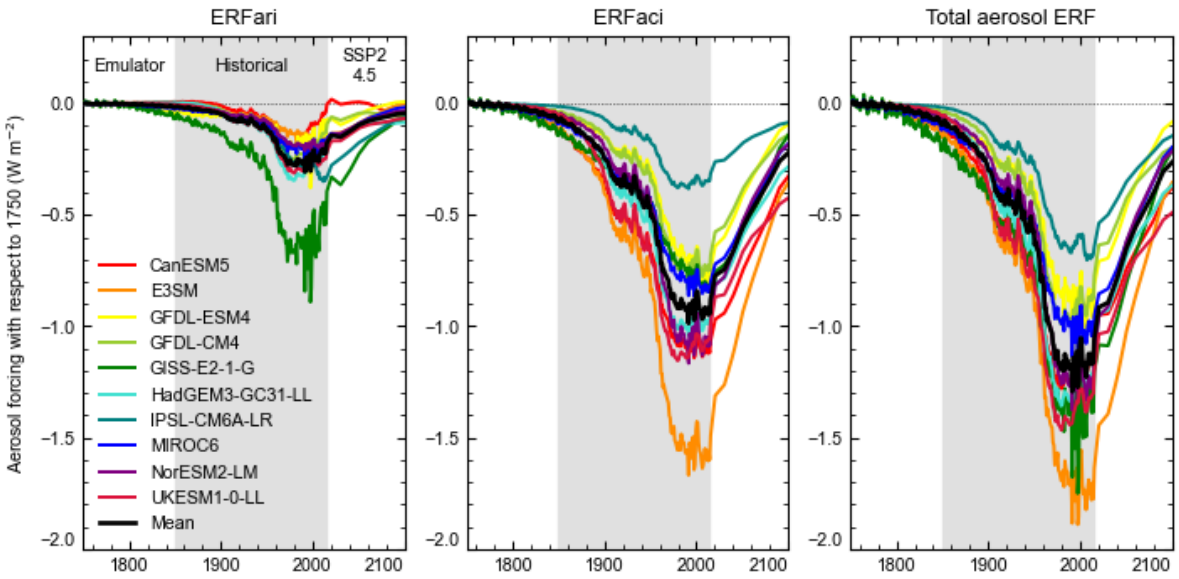

Figure 3: Emulated emissions to forcing curves, relative to 1750. The multi-model mean emulation is shown in black.

2.1.4 Ensemble generation

To simulate time-varying aerosol forcing we take probabilistic ensembles for both the magnitude and the shape of the historical aerosol forcing. To generate historical shapes, we take 25,000 samples of α_{SO2}, α_{BC}, α_{OC}, s_{SO2} and s_{BC+OC} based on their distributions from the 10 participating GCMs (Table 2). A joint kernel-density estimate of the α coefficients is used to derive a distribution which is then sampled from for ERFari (Fig. 4a-c). Accounting for correlation between the coefficients maintains the connection that different aerosol species are often co-emitted. For ERFaci, we take $\log(s_{SO2})$ and $\log(s_{BC+OC})$ from each model and derive a joint kernel distribution from these two parameters (Fig. 4d). Logarithms are used because the total ERFaci in Eq. (2) has a logarithmic relationship to emissions and individual model estimates of these parameters span several orders of magnitude. β is not a degree of freedom in this setup because the resultant ERFaci time series will be scaled as described below.

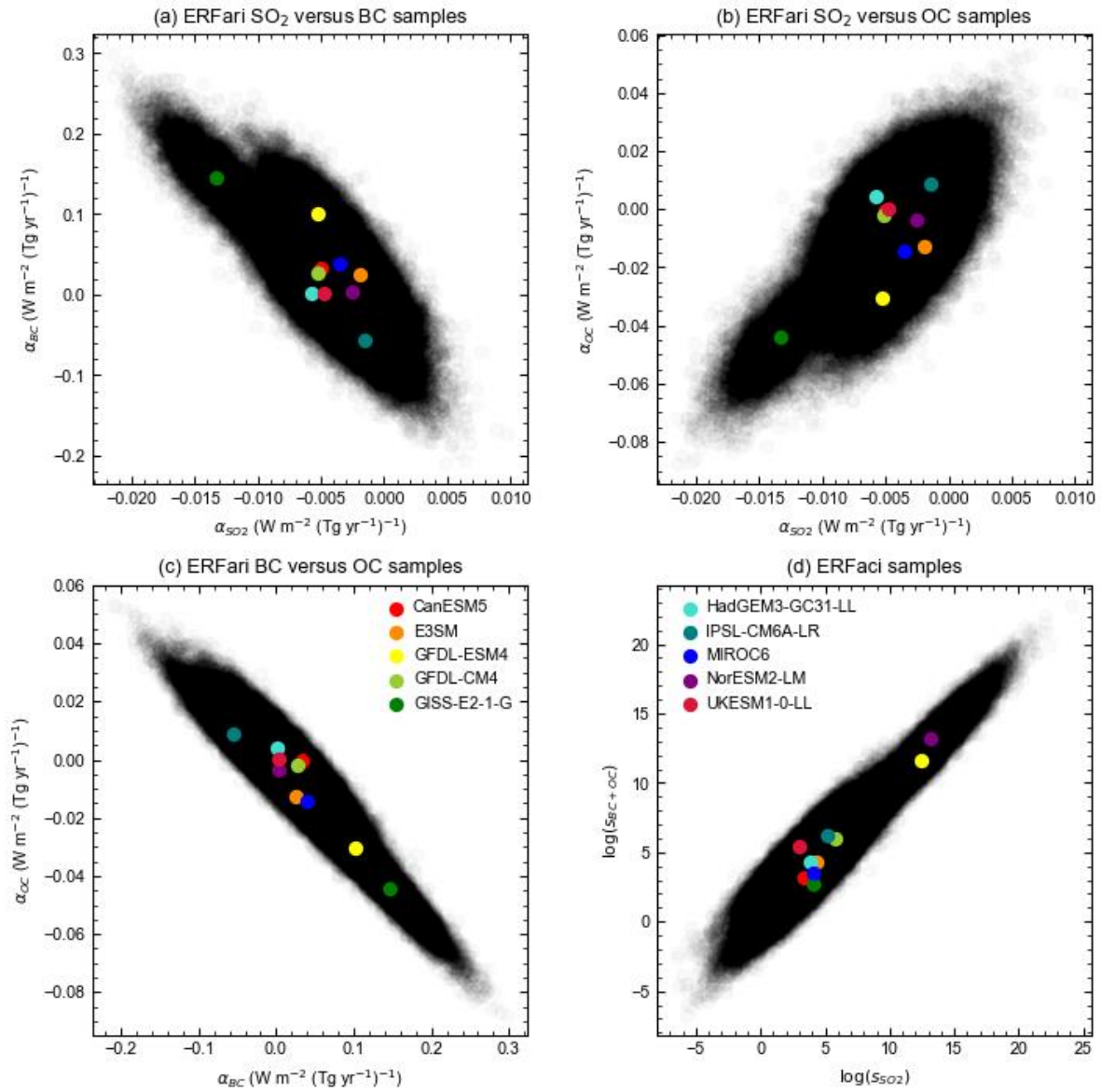

Figure 4: Joint distributions of (a) α_{SO2} and α_{BC}, (b) α_{SO2} and α_{OC}, (c) α_{BC} and α_{OC}, (d) $\log(s_{SO2})$ and $\log(s_{BC+OC})$. The cloud of points represent the 25000 drawn sample sets and the coloured points are fits to each CMIP6 model.

We combine the sampled α and s coefficients with 25,000 samples of the absolute values of the 1850 to 2005-15 ERFari and ERFaci from the process-based assessment in fig. 8 of Bellouin, Quaas, et al. (2020; hereafter the "Ringberg assessment"), using the distributions that do not account for energy budget constraints. This process rescales the α coefficients and selects β in each ensemble member consistent with the present-day ERFaci. These 25,000 sampled time series are then rebased to a 1750 baseline by subtracting the 1750 forcing from the 1850 forcing, producing 25,000 candidate historical time series of aerosol forcing for the period 1750-2019 that differ in shape and magnitude (Fig. 5).

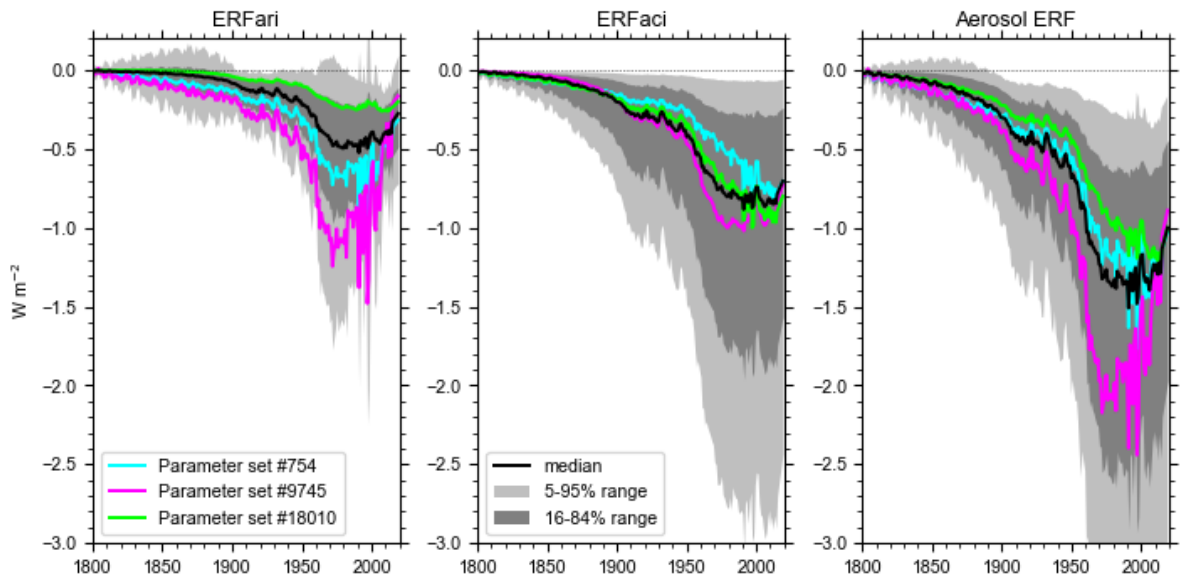

Figure 5: Sampled ERFari, ERFaci and total aerosol ERF time series before constraint. Overplotted are three individual ensemble members (coloured lines) that have present-day total aerosol forcing close to the ensemble mean with different time histories. The 5-95% and 16-84% ranges of the ensemble are shown as light and dark grey bands with the ensemble median in black.

2.1.5 Alternative historical datasets

In addition to the CMIP6 emissions which is the main focus of this study, we investigate an alternative emissions dataset from ECLIPSE, version 6b (Stohl et al., 2015) under current global air pollution legislation. We use the same forcing emulator with the same parameter sets for α and s as for the CMIP6 emissions, but substitute emissions from ECLIPSE v6b for 1990 to 2019. There is emerging evidence that emissions reductions in China, particularly of SO_2, occurred earlier and were more extensive than implied in the CEDS inventory (Kanaya et al., 2020; Paulot et al., 2018; Zheng et al., 2018), and the ECLIPSE dataset takes these reductions into account (Fig. S2). ECLIPSE data is provided in 5-year intervals from 1990 to 2020, and we use a linear interpolation between these data points to obtain annual emissions of OC, BC and SO_2. Up until 1980 we use the CEDS historical emissions and linearly transition between the two datasets over the 1980 to 1990 timeframe. ECLIPSE does not include emissions from aviation or biomass burning, so we revert to the aviation sector emissions from CEDS and biomass emissions from BB4CMIP.

Alongside the CMIP6 and ECLIPSE emissions-based aerosol forcing time series, we repeat the analyses using scaled historical ERFari and ERFaci from each CMIP6 model. We also use RFari and RFaci time series generated from the Oslo-CTM3 chemistry transport model (Lund et al., 2018, 2019) for 1750-2020 under SSP2-4.5. In these 10 CMIP6 models plus Oslo-CTM3, the magnitude of 1850 to 2005-15 forcing is allowed to vary according to the Ringberg assessment distributions, and the generated time series are extrapolated backwards to a 1750 baseline. Unlike the CMIP6 and ECLIPSE emissions time series run with the forcing emulator, the historical shapes of ERFari and ERFaci from these 11 model estimates are fixed.

2.2 Non-aerosol forcing time series

The non-aerosol component forcings are also generated from a 25,000-member Monte Carlo ensemble. As they are either less uncertain or smaller in magnitude (or both) than the aerosol forcing they are not the main focus of this paper but are generated to provide a consistent view of the total ERF, including uncertainty estimates, so that energy budget constraints can be applied. Detailed information is provided in Supplementary Text S1 with a summary of the key data sources in Table 3.

Table 3: Non-aerosol forcing present-day uncertainties and key references.

Forcing type	**Key references**
Well-mixed greenhouse gases	Etminan et al. (2016); Gidden et al. (2019); Hodnebrog et al. (2013); Meinshausen et al. (2017); Myhre, Shindell, et al. (2013); Smith et al. (2020); Smith, Kramer, et al. (2018)
Ozone	Checa-Garcia et al. (2018); Newman et al. (2007); Smith, Forster, et al. (2018); Stevenson et al. (2013)
Stratospheric water vapour from methane oxidation	Myhre, Shindell, et al. (2013)
Aviation contrails	Bickel et al. (2020); Bock & Burkhardt (2016); Gettelman & Chen (2013)
Black carbon on snow	Myhre, Shindell, et al. (2013)
Land-use change	Ghimire et al. (2014)
Volcanic	Global Volcanism Program (2013); Gregory et al. (2016); Kovilakam et al. (2020); Toohey & Sigl (2017)
Solar	Gray et al. (2009); Matthes et al. (2017); Smith, Kramer, et al., (2018); Vieira et al., (2011)

2.3 Simple climate model

We use our 25,000 member ensemble of aerosol and non-aerosol forcings and run them in a two-layer energy balance model, including efficacy of deep-ocean heat uptake (Geoffroy, Saint-Martin, Bellon, et al., 2013; Geoffroy, Saint-Martin, Olivié, et al., 2013; Held et al., 2010). To perform this many simulations precludes the use of a comprehensive GCM and similar constrained Monte Carlo ensemble methods using reduced-complexity models have been done previously (Meinshausen et al., 2009; Smith, Forster, et al., 2018). The structural uncertainty associated with the choice of simple climate model has been found to have limited impact on global mean temperature projections in historical simulations (Nicholls et al., 2020). We choose to use the two-layer model due to its computational efficiency, inclusion of both EEU and GSAT, and its proven ability as a useful emulator of complex GCMs (Palmer et al., 2018). We use the formulation from the two Geoffroy et al. papers, hereafter G13a and G13b. The two-layer model can be written as

$$C_{mix}\, dT_{mix}/dt \;= F - \lambda T_{mix} \;-\; \epsilon\gamma(T_{mix} - T_{deep}) \quad (3)$$

$$\epsilon C_{deep}\, dT_{deep}/dt \;= \epsilon\gamma(T_{mix} - T_{deep}) \quad (4)$$

where C_{mix} and C_{deep} (W yr m^{-2} K^{-1}) are the heat capacities of the ocean mixed layer and deep ocean, T_{mix} and T_{deep} (K) are the respective layer temperature anomalies, λ (W m^{-2} K^{-1}) is the climate feedback parameter, F (W m^{-2}) is the effective radiative forcing, ε (dimensionless) is the efficacy of deep ocean heat uptake and γ (W m^{-2} K^{-1}) the heat transport between the two layers.

The relatively small heat capacity of the land surface and atmosphere compared to the ocean means that it can be neglected and the GSAT anomaly is given by T_{mix}.

All available 44 CMIP6 models that published both abrupt-4xCO2 and piControl simulations to the Earth System Grid Foundation as of 2 July 2020 were used to tune the two-layer model using the method set out in G13a and G13b.The two-layer model is tuned to the GSAT and TOA radiation imbalance of each CMIP6 model's abrupt-4xCO2 run. There are five free parameters in the G13b model: γ, ε, λ, C_{mix} and C_{deep}. Radiative forcing from a quadrupling of CO_2 ($F_{4\times}$) is also calibrated using this method with the abrupt-4xCO2 experiments. Table S1 sets out the parameters for each model and Fig. S3 shows the temperature evolution in CMIP6 models for the model output and the simulated two-layer model fits for abrupt-4xCO2. The ECS is an emergent parameter from this model and is calculated as $F_{4\times}/-2\lambda$. The inclusion of the efficacy of ocean heat uptake in the two-layer model leads to different and often larger estimates of climate sensitivity than from a "Gregory regression" of TOA energy imbalance against global mean temperature anomaly for the first 150 years of abrupt-4xCO2 (the so-called "effective" climate sensitivity, EffCS). The strengthening of climate feedbacks over time as temperatures approach equilibrium in abrupt-4xCO2 experiments results in the long-term equilibrium ECS being in the region of 10-30% larger than EffCS (Rugenstein et al., 2020). The version of the two-layer model that includes efficacy of ocean heat uptake captures this effect somewhat, and we cautiously refer to our derived climate sensitivity as ECS for this reason.

A joint kernel density estimate distribution of the six input parameters to the two-layer model are sampled based on the calibrated CMIP6 model estimates (marginal distributions for each parameter are shown in Fig. S4). The joint distribution allows for correlation between model parameters to be taken into account when sampling (Table S2).

Internal variability in GSAT is simulated by analysing the piControl run in all available models (49 as of 2 July 2020). Global mean temperatures from the piControl simulations are detrended to remove any residual drift with the residuals around the long term trend taken to be the internal variability. The autocovariance matrix of these residuals in each model is constructed by regressing the time series with itself at lag 1, lag 2, …, lag *n* where *n* is the length of the model's piControl simulation. This input is then used as the covariance of a multivariate Gaussian distribution that governs the time-dependent internal variability of temperatures in each model. For each ensemble member simulated, one of the 49 CMIP6 models is selected at random, and 270 years (1750-2019) of internal variability generated based on the underlying distribution in the selected GCM. This allows for a more realistic construction of internal variability than a memoryless process noting that in reality events such as ENSO tend to cluster warm and cool years, and also provides for the recreation of low-frequency long-term internal variability that is present in some models such as CNRM-ESM2-1 (Fig. S5).

2.4 Observational constraints

We use GSAT estimates from 1850-2019 and total Earth system energy uptake observations from 1971-2018 to constrain our simulations. To estimate GSAT we use the Cowtan & Way (2014) dataset of infilled global-mean surface temperatures (GMST; near-surface temperatures over land and sea-ice and sea-surface temperatures over open ocean) for 1850-2019, multiplied by a time-varying ratio of GSAT/GMST from CMIP5 models under the

historical and RCP8.5 pathways from 1861 to 2014 (Richardson et al., 2016). This ratio converges towards 1.08 for the recent past (Rogelj et al., 2019) and we extend this ratio forward to 2019. Both observations and model output are rebased to the 1850-1900 mean as a proxy for pre-industrial following the IPCC Special Report on 1.5°C. This results in a central estimate of GSAT warming of 1.10°C for 2010-19 relative to 1850-1900.

For observations of total Earth energy uptake, we use data from the Global Climate Observing System (GCOS) observational dataset that includes estimates from ocean heat uptake, cryosphere, atmosphere and land surface (von Schuckmann et al., 2020). The ocean has absorbed 92% of the total energy uptake in the Earth system since 1960 owing to its larger thermal capacity compared to other components of the Earth system. The two-layer model only tracks heat uptake into the ocean, but to be physically consistent with the total observed EEU we assume that the heat uptake of the atmosphere, cryosphere and land is taken into account in the heat uptake of the mixed layer of the ocean. The GCOS dataset extends back to 1960, but we focus on the period from 1971-2018 due to the limited coverage of deep ocean temperature observations before the advent of expendable bathythermographs (XBTs) in the late 1960s (Palmer, 2017). Our constraint is based on the agreement of ocean heat uptake in the two-layer model with the total EEU from GCOS of 385 ± 47 ZJ, using 1971 and 2018 as start and end points, and taking the AR5 assessment uncertainty range (here expressed as one standard deviation).

Following the running of the two-layer model, each of the 25,000 ensemble members is assigned a weight w_i based on how well it reproduces GSAT and EEU observations. The weighting is based on the model weighting technique of Knutti et al. (2017):

$$w_i = \exp\left(-\left({r_{GSAT,i}}^2/{\sigma_{GSAT,D}}^2 + {r_{EEU,i}}^2/{\sigma_{EEU,D}}^2\right)\right) \quad (5)$$

where $r_{X,i}$ is a measure of how well the model reproduces observations for variable X for ensemble member i, and $\sigma_{X,D}$ is the "radius of model quality" (Sanderson et al., 2015). The radius of model quality is a subjective choice and for both GSAT and EEU we use assessed uncertainties. For GSAT, $r_{GSAT,i}$ represents the root-mean-square error (RMSE) of each ensemble member's simulated temperature compared to observations and $\sigma_{GSAT,D}$= 0.12°C based on the "likely" (> 66%) range of GMST from the 1850-1900 period to 2006-15 in IPCC Special Report on Global Warming of 1.5°C. For EEU, we use the AR5 uncertainty of $\sigma_{EEU,D}$= 47 ZJ. Unlike in Knutti et al. (2017) we do not downweight similar ensemble members.

Following calculation of each w_i, the ensemble weights are normalised such that $\sum w_i = 1$. Although subjective, our choices for the goodness-of-fit to the constraints ensure that GSAT and EEU have approximately equal influence on the total weighting given to each ensemble member (Fig. S6). An ensemble member will receive a high weight if it is close to both observed GSAT and observed EEU resulting in fewer, higher weight ensemble members than using a single constraint only. Results using just one constraint are reported in the supplementary material. The emissions-driven aerosol forcing time series will be referred to as SSP-constrained in the results.

3 Results

Figure 6 shows the aerosol ERF time series that best fit the observational constraints of GSAT and EEU for the 13 scenarios considered. Also shown are the projections of GSAT and EEU with the applied ensemble weighting. The weighted 5 to 95% range from the CMIP6-constrained time series using both GSAT and EEU as constraints is shown as a grey band with the weighted mean as a grey line. The 1750-2019 aerosol ERF is determined to be -0.89 W m^{-2} (-1.49 to -0.37 W m^{-2} 5-95% range), comprised from -0.27 (-0.60 to -0.07) W m^{-2} for ERFari and -0.59 (-1.17 to -0.13) W m^{-2} for ERFaci. The central estimate of total aerosol forcing is close to the -0.9 (-1.9 to -0.1) W m^{-2} assessed for 1750-2011 in AR5, with a narrower "very likely" (> 90%) range.

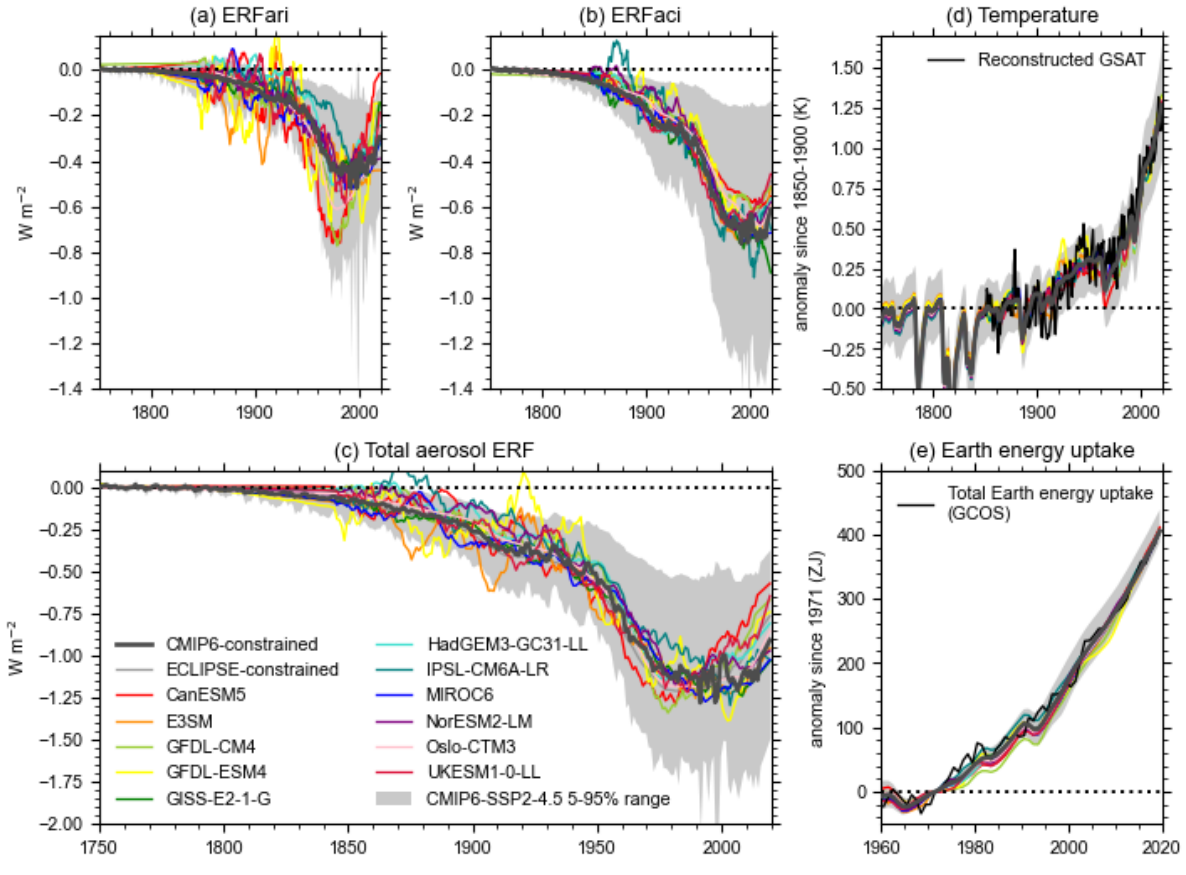

Figure 6: Weighted historical time series using (a) ERFari, (b) ERFaci and (c) total aerosol ERF time history shapes from each forcing scenario. Curves derived from CMIP6 models and Oslo-CTM3 are scaled and ensemble-weighted as described in section 2 and do not represent raw model output. (d) and (e) shows the weighted ensemble simulated global mean surface temperature and ocean heat uptake. Solid lines are weighted ensemble means and shaded regions show the weighted 5th-95th percentiles for the CMIP6-constrained time series.

With the CMIP6-constrained time series, aerosol ERF is relatively constant between 1972 and 2014, with a mean of -1.13 W m^{-2} relative to 1750. The mean aerosol forcing for the 2005-14 period is -1.12 (-1.75 to -0.53) W m^{-2}. However, this result is sensitive to the underlying emissions inventory. Using ECLIPSE emissions, 2005-14 aerosol ERF is -0.97 (-1.58 to -0.44)

W m^{-2} relative to 1750, and -0.72 (-1.37 to -0.26) W m^{-2} in 2019. Given that the forcing emulator was trained on CMIP6 emissions, we retain the CMIP6-constrained time series as our primary estimate. It can be inferred that the CMIP6-constrained time series favours an approximately constant or slightly negative-trending aerosol forcing over recent decades (fig. 7) indicated by the portion of the prior distribution constrained out by the observations. This is in contrast to 7 out of the 10 CMIP6 models which show an increase in (positive) aerosol forcing since 1980. A rapid recovery in aerosol forcing simulated by the UKESM1-0-LL model for example is not favoured by the energy budget constraints, whereas aerosol forcing shapes simulated by two of the three models with a slight negative 1980-2014 aerosol forcing trend, GISS-E2-1-G (green) and MIROC6 (blue), show good correspondence to the CMIP6-constrained central estimate.

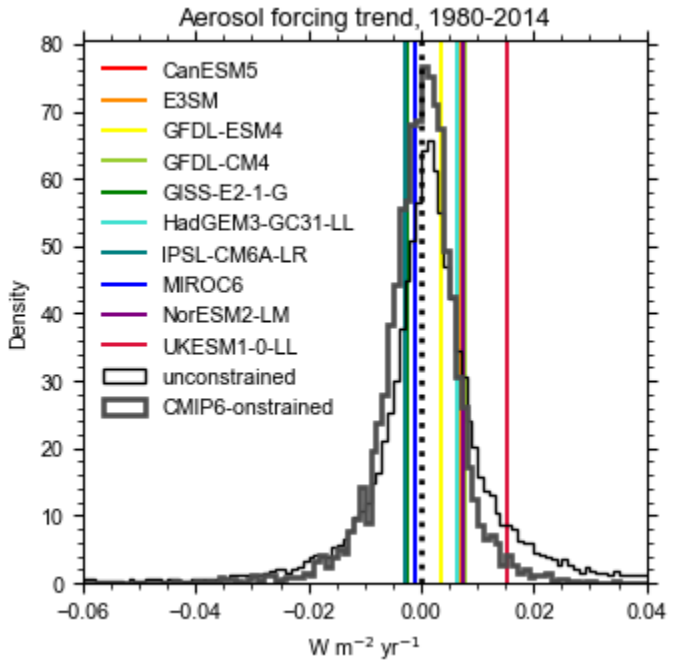

Figure 7: Histograms of linear aerosol forcing trends for 1980-2014 simulated by the 25,000 member Monte Carlo ensemble (thin black histogram) and weighted after application of observational constraints in the CMIP6-constrained time series (thick grey histogram). The trends of each CMIP6 model's aerosol forcing are shown in coloured lines. CanESM5, E3SM, GFDL-CM4, HadGEM3-GC31-LL and NorESM2-LM are clustered near +0.007 W m^{-2} yr^{-1}.

Figure 8 uses the GSAT and EEU constraints to show the present-day distributions of aerosol forcing. Alongside this we use the ensemble weights to calculate distributions of ECS and TCR from the ensemble given the two-layer model parameter distributions and ensemble weights. To calculate TCR we use the same parameter setups in each of the 25,000 ensemble members and simulate the forcing from a 1% per year compound CO_2 increase taking TCR as the 21-year mean of warming in years 60-80. The median, 68% and 90% range for these parameters along with their unconstrained (prior) distributions are shown in Table 4. All 13 historical time series are shown in Table S3 for both GSAT and EEU constraints, and in Tables S4 and S5 using only GSAT or EEU respectively.

A diversity of constrained present-day aerosol ERF distribution shapes is possible for the aerosol forcing from each model's historical time evolution. In particular there are a group of models (the two from GFDL, HadGEM3-GC31-LL and GISS-E2-1-G) where present-day ERFari is relatively weak and no values less than -0.5 W m^{-2} satisfy the observational constraints, but all models except E3SM result in a less negative distribution than the Ringberg assessment which is reflected in the CMIP6-constrained distribution. For ERFaci, neither the CMIP6 models nor the CMIP6-constrained time series support a strong negative forcing and the constrained distributions are less skewed than the Ringberg assessment range. All historical aerosol forcing time series constrain the present-day aerosol forcing to a narrower range than the full process-based distributions of the Ringberg assessment. As discussed in Bellouin, Quaas, et al. (2020), energy budget constraints do not favour a present-day aerosol forcing more negative than -2 W m^{-2}, and this is also borne out by our distributions in Fig. 8c.

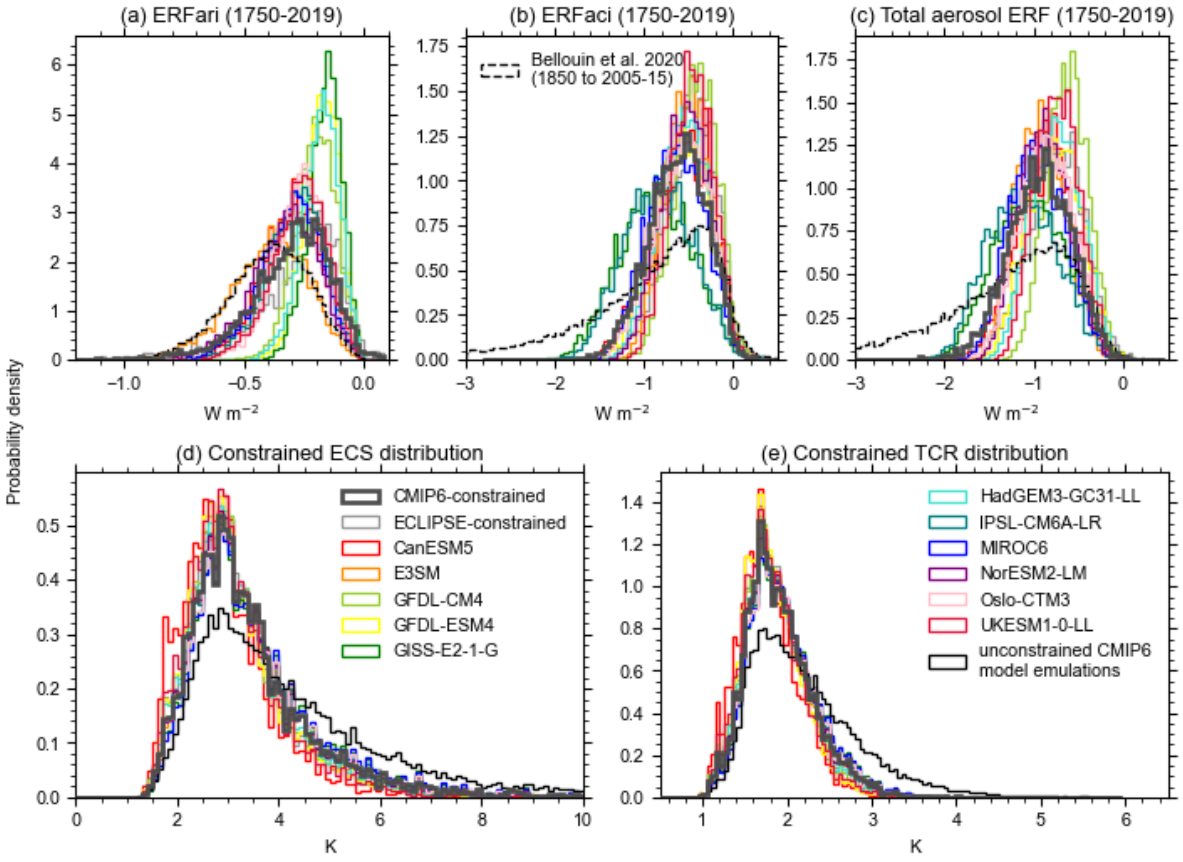

Figure 8: Distributions of (a) ERFari, (b) ERFaci, (c) total aerosol ERF, (d) ECS and (e) TCR. Thin black curves show the prior distributions for aerosol forcing, ECS and TCR.

High values of ECS and TCR are also constrained out when applying observational constraints (Fig. 8d,e). The prior distributions in thin black curves allow for ECS values much larger than those seen in CMIP6 models as values of net feedback λ sampled in the prior distribution (Fig. S4) can be close to zero. Interestingly, the choice of historical aerosol forcing time series is less important for constraining ECS and especially TCR than for the present-day

aerosol forcing, and in every case the constrained distribution favours lower climate sensitivity than the CMIP6-derived prior. The constrained distribution of ECS is not tight, especially at the upper end (1.9 to 6.0°C 5-95% range with a best estimate of 3.1°C), which is marginally lower than the raw CMIP6 model range inferred from the two-layer model fits (2.0 to 6.6°C; Table S1). Transient climate response falls in the 5-95% range of 1.3 to 2.7°C (best estimate 1.8°C).

Table 4: Ensemble percentiles for aerosol forcing, ECS and TCR, for the CMIP6-informed constrained and the prior (unconstrained) distributions.

		5%	**16%**	**50%**	**84%**	**95%**
Total Aerosol ERF 1750-2019 (W m^{-2})	**Constrained**	-1.49	-1.25	-0.89	-0.56	-0.37
	Unconstrained	-2.98	-1.97	-1.00	-0.44	-0.17
ERFari 1750-2019 (W m^{-2})	**Constrained**	-0.60	-0.45	-0.27	-0.14	-0.07
	Unconstrained	-0.72	-0.49	-0.27	-0.11	0.10
ERFaci 1750-2019 (W m^{-2})	**Constrained**	-1.17	-0.93	-0.59	-0.29	-0.13
	Unconstrained	-2.43	-1.56	-0.70	-0.24	-0.05
ECS (°C)	**Constrained**	1.93	2.35	3.13	4.44	5.99
	Unconstrained	2.10	2.56	3.73	6.11	8.98
TCR (°C)	**Constrained**	1.34	1.53	1.85	2.29	2.68
	Unconstrained	1.43	1.61	2.08	2.80	3.45

Figure 9 shows the CMIP6-constrained time series plotted against each CMIP6 model's ERF time series, where the 1750 to 1850 aerosol ERF is filled in using the forcing emulator with model-specific curve fits (Table 2). To each model's forcing time series an 11-year Savitzky-Golay smoothing filter is applied for ease of comparison. We also show an observational estimate from MERRA2 for RFari+aci, using the methods described in Bellouin, Davies, et al. (2020) (note this does not include any rapid adjustment). For the 10 CMIP6 models, two (UKESM1-0-LL and E3SM) have an aerosol forcing below the 5th percentile of the CMIP6-constrained range for most of the 20th Century, and most models show an aerosol recovery starting around 1975 or earlier that is not seen in the observations. MIROC6 (blue) produces an aerosol forcing time series that is approximately consistent with energy budget constraints across the full historical period and is consistent with the observations in that it does not produce a substantial recovery of aerosol forcing in recent years. Although 10 models is a relatively small subset of CMIP6, there is some evidence from these models that aerosol forcing over the mid-to-late 20th Century may be too negative, and the recovery in aerosol forcing since 1975 has been overstated, or both.

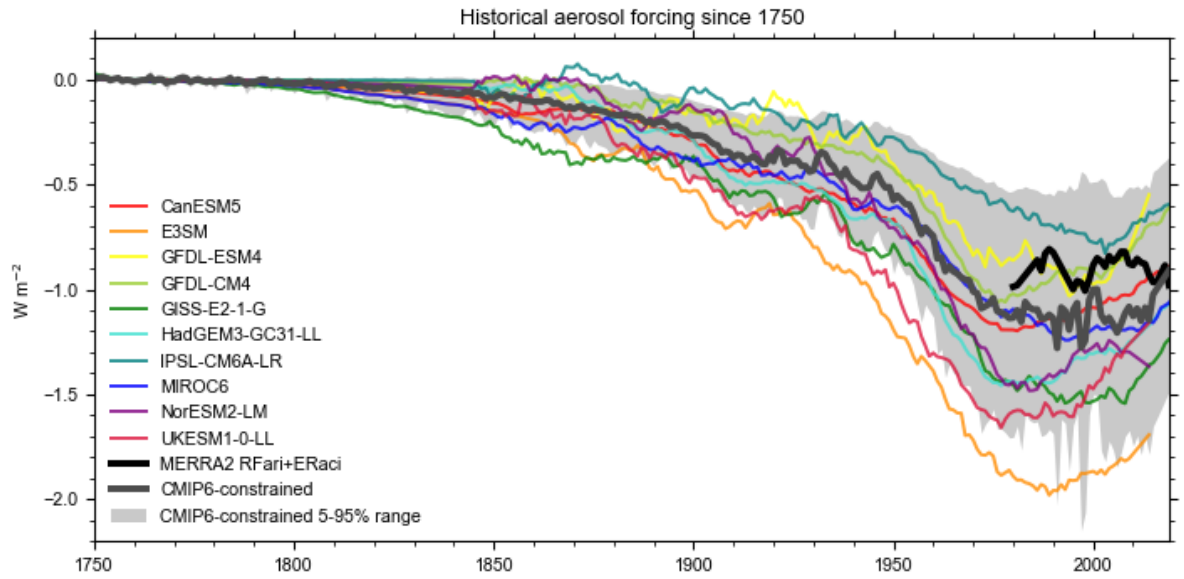

Figure 9: Smoothed 1750-2019 aerosol forcing from each CMIP6 model (thin coloured lines), plotted relative to the CMIP6-constrained best estimate time series (thick grey line) and 5-95% range (shaded grey area). Also shown is the observational estimate of RFari+aci (thick black line) based on MERRA2 reanalysis (Bellouin, Davies, et al., 2020). CMIP6 models are shown as smoothed 1850 to 2014 (or 2019 where SSP2-4.5 was run) and extended back to 1750 using the emissions to forcing emulator with model-specific curve fits (section 2.1.3).

4 Discussion and conclusions

Comprehensive climate models are the best tools available for determining global aerosol forcing, for which global observations do not exist prior to the satellite era (approximately 1980). However, model-derived aerosol forcing depends on a chain of processes, and ultimately on spatially-resolved aerosol precursor emissions time series that are themselves uncertain (Hoesly et al., 2018). It is not possible to determine here whether the tendency for some models to project strong aerosol forcing in the second half of the 20th Century and/or too much of a recent aerosol recovery, at least compared to what would be implied by the observational constraints, is due to model processes or uncertainties in the precursor emissions. However, using the energy balance framework described in this paper with a simple forcing emulator (eqs. (1) and (2)), climate-model derived forcing can be corrected to better match historical observations.

One limitation of the forcing emulator to derive the CMIP6-constrained forcing estimates is the sensitivity to changes in the emissions, which is seen from the large reduction in SO_2 in SSP2-4.5 in 2015. However, this SO_2 jump is also present in the forcing simulated by Oslo-CTM3, and correspondence between our timeseries and the one from Lund et al. (2019) after scaling to match the energy budget constraints is good, showing that the simple forcing emulator presented in this paper can adequately simulate the global mean aerosol ERF from a complex process-based chemistry transport model (Fig. S7). The alternative emissions data from ECLIPSE v6b with the forcing emulator shows more of a recovery and a less negative present-day aerosol forcing that the CMIP6-constrained time series, and the differences are mostly due to an earlier reduction in emissions from China which is supported by observations. It is unclear how GCMs would respond to these greater emissions reductions had they been run with the

ECLIPSE emissions rather than CMIP6 dataset. Observational evidence suggests that global aerosol forcing has been relatively constant from 1980 to 2019 (Fig. 9; Bellouin, Davies, et al., 2020). The forcing emulator is trained on how GCMs respond to CMIP6 emissions for global forcing, so may have produced a different set of coefficients if it was fit to GCM output run with ECLIPSE emissions. It is likely that regional effects are significant and aerosols emitted from different source regions affect the global energy balance in different ways which is not captured in a global emissions to forcing relationship (Kretzschmar et al., 2017). Including how global forcing changes to regional aerosol emissions could be an improvement to the forcing emulator, although may be difficult to implement for aerosol-cloud interactions in marine stratocumulus cloud decks which may be thousands of kilometres from the emissions source (Regayre et al., 2014). However, we show for the 10 GCMs that our relationship is trained on, the forcing emulator works well (Fig. 2) and is useful as a first-order global relationship that incorporates sufficient flexibility in its forcing response to emissions.

Our results are consistent with the conclusions of previous studies that have attempted to constrain present-day aerosol forcing based on energy balance arguments. We find that very large negative values of pre-industrial to present-day aerosol ERF are inconsistent with observed warming and total Earth system energy gain (Andrews & Forster, 2020; Forest, 2018; Forest et al., 2002, 2006; Skeie et al., 2018; Smith, Forster, et al., 2018). Our best estimate 1750-2019 aerosol forcing of -0.89 W m^{-2} is similar to recent observationally-constrained studies that put aerosol forcing in the -0.8 to -0.9 W m^{-2} range (Andrews & Forster, 2020; Skeie et al., 2018; Smith, Forster, et al., 2018), and the review of 19 inverse estimates in Forest (2018) of -0.77 W m^{-2}. Our estimate for 1972-2014 of -1.12 W m^{-2} is also similar to the 1970-2000 estimate of -1.06 W m^{-2} of Murphy et al. (2009). We also find that the most likely shape of recent (1980-2014) aerosol forcing is approximately constant or with a slightly negative trend, which is in line with satellite-derived estimates of aerosol RFari and RFaci (Bellouin, Davies, et al., 2020). Beyond 2014, the forcing emulator is not able to reproduce the observations due to the rapid decline in SO_2. However, the MERRA2 reanalysis, which provides the data to apply the methods of Bellouin, Davies, et al. (2020) applied in this work, shows increases in natural dust and sea-salt aerosols over the last decade which would compensate for a reduction in anthropogenic forcing.

The shape of historical aerosol forcing time series - whether from our simple emulator or provided by a particular CMIP6 model - does not provide a constraint on the overall 1750-2019 aerosol forcing. However, the choice of aerosol forcing dataset used matters less for constraining ECS and TCR than it does for the shape or magnitude of present-day forcing (Fig. 8). It is difficult to constrain the upper bound of ECS due to the heavy tail of the prior distribution, and 95th percentile values of ECS range from 4.7 to 6.4°C depending on the aerosol forcing time series used (Table S3). Other studies also show that these constrained climate sensitivity distributions are sensitive to the priors used (Sherwood et al., 2020). For example, our prior sample space informed by CMIP6 models has very few ensemble members with ECS < 1.5°C and TCR < 1.0°C, both lower bounds of the respective “likely” range in AR5, and it is possible that this area of the distribution is undersampled. Note that we do not perform a full Bayesian analysis in this paper. However, our ECS estimate of 3.1°C (1.9 to 6.0°C) is in line with, although with wider uncertainty, than the Bayesian estimate for EffCS of 3.2 (2.3 to 4.7°C) in Sherwood et al. (2020), which takes into account several lines of evidence in their assessment.

Our results suggest that the limited number of CMIP6 models considered here have a stronger aerosol forcing than may have actually occurred during the 20th Century (Fig. 9) and this effect may be responsible for the modest warming in the CMIP6 ensemble mean over this time period (0.20 ± 0.22°C for 1961-90 relative to 1850-1900 in CMIP6 models compared to reconstructed GSAT observations of 0.39 ± 0.06°C over the same period; Fig. S8). The diagnosis of historical aerosol forcing in more CMIP6 models to confirm or disprove this would be welcomed. Inclusion of uncertainties in historical emissions would be useful to determine whether this is a factor in suppression of warming; for example, it was recently noted that SO_2 emissions over the US were overstated by 22% in the CEDS timeseries in the 1960s (https://github.com/JGCRI/CEDS/issues/3). Re-running of GCMs with updated emissions inventories could determine how sensitive models are to emissions uncertainties, and the importance of regional effects. The time history of aerosol forcing and its present-day magnitude both constrain key climate system uncertainties such as climate sensitivity and the rate of recent warming (Tanaka & Raddatz, 2011). Reducing uncertainty in both will reduce uncertainty in climate projections.

Acknowledgments and Data

We thank Tim Andrews and Adriana Sima for provision of prototype versions of the HadGEM3-GC3.1-LL and IPSL-CM6A-LR model outputs respectively, Zbigniew Klimont for provision of the ECLIPSE emissions data and Bill Collins (U. Reading) for valuable feedback on the manuscript draft. We acknowledge the World Climate Research Programme, which, through its Working Group on Coupled Modelling, coordinated and promoted CMIP6. We thank the climate modeling groups for producing and making available their model output, the Earth System Grid Federation (ESGF) for archiving the data and providing access, and the multiple funding agencies who support CMIP6 and ESGF. C.J.S. was supported by a NERC/IIASA Collaborative Research Fellowship (NE/T009381/1). P.M.F. and C.J.S were supported by European Union's Horizon 2020 Research and Innovation Programme under grant agreement nos. 820829 (CONSTRAIN) and UKRI NERC grant NE/N006038/1 (SMURPHS). G.H. and M.R. were supported by the Joint UK BEIS/Defra Met Office Hadley Centre Climate Programme (GA01101). The Energy Exascale Earth System Model (E3SM) is funded by the U.S. Department of Energy, Office of Science, Office of Biological and Environmental Research. Work at LLNL was performed under the auspices of the U.S. Department of Energy by Lawrence Livermore National Laboratory under contract DE-AC52-07NA27344.

The two layer climate model will be made available on a GitHub repository and the APRP code is available from https://github.com/chrisroadmap/climateforcing/. All code used in the paper will be available at Zenodo and a DOI produced. Cowtan & Way temperature observations are available at https://www-users.york.ac.uk/~kdc3/papers/coverage2013/had4_krig_annual_v2_0_0.txt. GCOS Earth system energy observations are available from https://doi.org/10.26050/WDCC/GCOS_EHI_EXP. CMIP6 model data used in this paper is available from the Earth System Grid foundation at https://esgf-node.llnl.gov/search/cmip6/, except the piClim-histaer runs from HadGEM3-GC3.1-LL and IPSL-CM6A-LR which are forthcoming. Model data from the E3SM AMIP pre-industrial aerosol experiment is available from https://esgf-node.llnl.gov/projects/e3sm/

References

Andrews, T., & Forster, P. M. (2020). Energy budget constraints on historical radiative forcing. *Nature Climate Change*, *10*(4), 313–316. https://doi.org/10.1038/s41558-020-0696-1

Bellouin, N., Quaas, J., Gryspeerdt, E., Kinne, S., Stier, P., Watson-Parris, D., et al. (2020). Bounding Global Aerosol Radiative Forcing of Climate Change. *Reviews of Geophysics*, *58*(1), e2019RG000660. https://doi.org/10.1029/2019RG000660

Bellouin, N., Davies, W., Shine, K. P., Quaas, J., Mülmenstädt, J., Forster, P. M., et al. (2020). Radiative forcing of climate change from the Copernicus reanalysis of atmospheric composition. *Earth System Science Data*, *12*(3), 1649–1677. https://doi.org/10.5194/essd-12-1649-2020

Bickel, M., Ponater, M., Bock, L., Burkhardt, U., & Reineke, S. (2020). Estimating the Effective Radiative Forcing of Contrail Cirrus. *Journal of Climate*, *33*(5), 1991–2005. https://doi.org/10.1175/JCLI-D-19-0467.1

Bock, L., & Burkhardt, U. (2016). Reassessing properties and radiative forcing of contrail cirrus using a climate model. *Journal of Geophysical Research: Atmospheres*, *121*(16), 9717–9736. https://doi.org/10.1002/2016JD025112

Booth, B. B. B., Harris, G. R., Jones, A., Wilcox, L., Hawcroft, M., & Carslaw, K. S. (2018). Comments on "Rethinking the Lower Bound on Aerosol Radiative Forcing." *Journal of Climate*, *31*(22), 9407–9412. https://doi.org/10.1175/JCLI-D-17-0369.1

Boucher, O., Servonnat, J., Albright, A. L., Aumont, O., Balkanski, Y., Bastrikov, V., et al. (n.d.). Presentation and evaluation of the IPSL-CM6A-LR climate model. *Journal of Advances in Modeling Earth Systems*.

Carslaw, K. S., Lee, L. A., Reddington, C. L., Pringle, K. J., Rap, A., Forster, P. M., et al. (2013). Large contribution of natural aerosols to uncertainty in indirect forcing. *Nature*, *503*(7474), 67–71. https://doi.org/10.1038/nature12674

Charlson, R. J., Schwartz, S. E., Hales, J. M., Cess, R. D., Coakley, J. A., Hansen, J. E., & Hofmann, D. J. (1992). Climate Forcing by Anthropogenic Aerosols. *Science*, *255*(5043), 423–430. https://doi.org/10.1126/science.255.5043.423

Checa-Garcia, R., Hegglin, M. I., Kinnison, D., Plummer, D. A., & Shine, K. P. (2018). Historical Tropospheric and Stratospheric Ozone Radiative Forcing Using the CMIP6 Database. *Geophysical Research Letters*, *45*(7), 3264–3273. https://doi.org/10.1002/2017GL076770

Collins, W. J., Lamarque, J.-F., Schulz, M., Boucher, O., Eyring, V., Hegglin, M. I., et al. (2017). AerChemMIP: quantifying the effects of chemistry and aerosols in CMIP6. *Geoscientific Model Development*, *10*(2), 585–607. https://doi.org/10.5194/gmd-10-585-2017

Cowtan, K., & Way, R. G. (2014). Coverage bias in the HadCRUT4 temperature series and its impact on recent temperature trends. *Quarterly Journal of the Royal Meteorological Society*, *140*(683), 1935–1944. https://doi.org/10.1002/qj.2297

Etminan, M., Myhre, G., Highwood, E. J., & Shine, K. P. (2016). Radiative forcing of carbon dioxide, methane, and nitrous oxide: A significant revision of the methane radiative forcing.

Geophysical Research Letters, *43*(24), 12,614-12,623. https://doi.org/10.1002/2016GL071930

Forest, C. E. (2018). Inferred Net Aerosol Forcing Based on Historical Climate Changes: a Review. *Current Climate Change Reports*, *4*(1), 11–22. https://doi.org/10.1007/s40641-018-0085-2

Forest, C. E., Stone, P. H., Sokolov, A. P., Allen, M. R., & Webster, M. D. (2002). Quantifying uncertainties in climate system properties with the use of recent climate observations. *Science*, *295*(5552), 113–117. https://doi.org/10.1126/science.1064419

Forest, C. E., Stone, P. H., & Sokolov, A. P. (2006). Estimated PDFs of climate system properties including natural and anthropogenic forcings. *Geophysical Research Letters*, *33*(1), n/a-n/a. https://doi.org/10.1029/2005GL023977

Forster, P. M., Richardson, T., Maycock, A. C., Smith, C. J., Samset, B. H., Myhre, G., et al. (2016). Recommendations for diagnosing effective radiative forcing from climate models for CMIP6. *Journal of Geophysical Research*, *121*(20), 12,460-12,475. https://doi.org/10.1002/2016JD025320

Geoffroy, O., Saint-Martin, D., Olivié, D. J. L., Voldoire, A., Bellon, G., & Tytéca, S. (2013). Transient Climate Response in a Two-Layer Energy-Balance Model. Part I: Analytical Solution and Parameter Calibration Using CMIP5 AOGCM Experiments. *Journal of Climate*, *26*(6), 1841–1857. https://doi.org/10.1175/JCLI-D-12-00195.1

Geoffroy, O., Saint-Martin, D., Bellon, G., Voldoire, A., Olivié, D. J. L., & Tytéca, S. (2013). Transient Climate Response in a Two-Layer Energy-Balance Model. Part II: Representation of the Efficacy of Deep-Ocean Heat Uptake and Validation for CMIP5 AOGCMs. *Journal of Climate*, *26*(6), 1859–1876. https://doi.org/10.1175/JCLI-D-12-00196.1

Gettelman, A., & Chen, C. (2013). The climate impact of aviation aerosols. *Geophysical Research Letters*, *40*(11), 2785–2789. https://doi.org/10.1002/grl.50520

Ghan, S. J. (2013). Technical Note: Estimating aerosol effects on cloud radiative forcing. *Atmospheric Chemistry and Physics*, *13*(19), 9971–9974. https://doi.org/10.5194/acp-13-9971-2013

Ghan, S. J., Smith, S. J., Wang, M., Zhang, K., Pringle, K., Carslaw, K., et al. (2013). A simple model of global aerosol indirect effects. *Journal of Geophysical Research: Atmospheres*, *118*(12), 6688–6707. https://doi.org/10.1002/jgrd.50567

Ghimire, B., Williams, C. A., Masek, J., Gao, F., Wang, Z., Schaaf, C., & He, T. (2014). Global albedo change and radiative cooling from anthropogenic land cover change, 1700 to 2005 based on MODIS, land use harmonization, radiative kernels, and reanalysis. *Geophysical Research Letters*, *41*(24), 9087–9096. https://doi.org/10.1002/2014GL061671

Gidden, M. J., Riahi, K., Smith, S. J., Fujimori, S., Luderer, G., Kriegler, E., et al. (2019). Global emissions pathways under different socioeconomic scenarios for use in CMIP6: a dataset of harmonized emissions trajectories through the end of the century. *Geoscientific Model Development*, *12*(4), 1443–1475. https://doi.org/10.5194/gmd-12-1443-2019

Global Volcanism Program. (2013). Volcanoes of the World v.4.9.0. Smithsonian Institution. https://doi.org/10.5479/si.GVP.VOTW4-2013

Golaz, J.-C., Caldwell, P. M., Van Roekel, L. P., Petersen, M. R., Tang, Q., Wolfe, J. D., et al. (2019). The DOE E3SM Coupled Model Version 1: Overview and Evaluation at Standard Resolution. *Journal of Advances in Modeling Earth Systems*, *11*(7), 2089–2129. https://doi.org/10.1029/2018MS001603

Gray, L. J., Rumbold, S. T., & Shine, K. P. (2009). Stratospheric Temperature and Radiative Forcing Response to 11-Year Solar Cycle Changes in Irradiance and Ozone. *Journal of the Atmospheric Sciences*, *66*(8), 2402–2417. https://doi.org/10.1175/2009JAS2866.1

Gregory, J. M., Andrews, T., Good, P., Mauritsen, T., & Forster, P. M. (2016). Small global-mean cooling due to volcanic radiative forcing. *Climate Dynamics*, *47*(12), 3979–3991. https://doi.org/10.1007/s00382-016-3055-1

Held, I. M., Winton, M., Takahashi, K., Delworth, T., Zeng, F., & Vallis, G. K. (2010). Probing the Fast and Slow Components of Global Warming by Returning Abruptly to Preindustrial Forcing. *Journal of Climate*, *23*(9), 2418–2427. https://doi.org/10.1175/2009JCLI3466.1

Held, I. M., Guo, H., Adcroft, A., Dunne, J. P., Horowitz, L. W., Krasting, J., et al. (2019). Structure and Performance of GFDL's CM4.0 Climate Model. *Journal of Advances in Modeling Earth Systems*, *11*(11), 3691–3727. https://doi.org/10.1029/2019MS001829

Hodnebrog, Ø., Etminan, M., Fuglestvedt, J. S., Marston, G., Myhre, G., Nielsen, C. J., et al. (2013). Global warming potentials and radiative efficiencies of halocarbons and related compounds: A comprehensive review. *Reviews of Geophysics*, *51*(2), 300–378. https://doi.org/10.1002/rog.20013

Hoesly, R. M., Smith, S. J., Feng, L., Klimont, Z., Janssens-Maenhout, G., Pitkanen, T., et al. (2018). Historical (1750–2014) anthropogenic emissions of reactive gases and aerosols from the Community Emissions Data System (CEDS). *Geoscientific Model Development*, *11*(1), 369–408. https://doi.org/10.5194/gmd-11-369-2018

Johnson, B. T., Haywood, J. M., & Hawcroft, M. K. (2019). Are Changes in Atmospheric Circulation Important for Black Carbon Aerosol Impacts on Clouds, Precipitation, and Radiation? *Journal of Geophysical Research: Atmospheres*, *124*(14), 7930–7950. https://doi.org/10.1029/2019JD030568

Kanaya, Y., Yamaji, K., Miyakawa, T., Taketani, F., Zhu, C., Choi, Y., et al. (2020). Rapid reduction in black carbon emissions from China: evidence from 2009–2019 observations on Fukue Island, Japan. *Atmospheric Chemistry and Physics*, *20*(11), 6339–6356. https://doi.org/10.5194/acp-20-6339-2020

Kelley, M., Schmidt, G. A., Nazarenko, L., Miller, R. L., Bauer, S. E., Ruedy, R., et al. (n.d.). GISS-E2.1: Configurations and climatology. *J. Adv. Model. Earth Syst., submitted*.

Knutti, R., Sedláček, J., Sanderson, B. M., Lorenz, R., Fischer, E. M., & Eyring, V. (2017). A climate model projection weighting scheme accounting for performance and interdependence. *Geophysical Research Letters*, *44*(4), 1909–1918. https://doi.org/10.1002/2016GL072012

Kovilakam, M., Thomason, L., Ernest, N., Rieger, L., Bourassa, A., & Millán, L. (2020). A Global Space-based Stratospheric Aerosol Climatology (Version 2.0): 1979--2018. *Earth System Science Data Discussions*, *2020*, 1–41. https://doi.org/10.5194/essd-2020-56

Kretzschmar, J., Salzmann, M., Mülmenstädt, J., Boucher, O., & Quaas, J. (2017). Comment on "Rethinking the Lower Bound on Aerosol Radiative Forcing." *Journal of Climate*, *30*(16), 6579–6584. https://doi.org/10.1175/JCLI-D-16-0668.1

Lund, M. T., Myhre, G., Haslerud, A. S., Skeie, R. B., Griesfeller, J., Platt, S. M., et al. (2018). Concentrations and radiative forcing of anthropogenic aerosols from 1750 to 2014 simulated with the Oslo CTM3 and CEDS emission inventory. *Geoscientific Model Development*, *11*(12), 4909–4931. https://doi.org/10.5194/gmd-11-4909-2018

Lund, M. T., Myhre, G., & Samset, B. H. (2019). Anthropogenic aerosol forcing under the Shared Socioeconomic Pathways. *Atmospheric Chemistry and Physics*, *19*(22), 13827–13839. https://doi.org/10.5194/acp-19-13827-2019

Mahajan, S., Evans, K. J., Hack, J. J., & Truesdale, J. E. (2013). Linearity of Climate Response to Increases in Black Carbon Aerosols. *Journal of Climate*, *26*(20), 8223–8237. https://doi.org/10.1175/JCLI-D-12-00715.1

van Marle, M. J. E., Kloster, S., Magi, B. I., Marlon, J. R., Daniau, A.-L., Field, R. D., et al. (2017). Historic global biomass burning emissions for CMIP6 (BB4CMIP) based on merging satellite observations with proxies and fire models (1750–2015). *Geoscientific Model Development*, *10*(9), 3329–3357. https://doi.org/10.5194/gmd-10-3329-2017

Matthes, K., Funke, B., Andersson, M. E., Barnard, L., Beer, J., Charbonneau, P., et al. (2017). Solar forcing for CMIP6 (v3.2). *Geoscientific Model Development*, *10*(6), 2247–2302. https://doi.org/10.5194/gmd-10-2247-2017

Meinshausen, M., Meinshausen, N., Hare, W., Raper, S. C. B., Frieler, K., Knutti, R., et al. (2009). Greenhouse-gas emission targets for limiting global warming to 2 °C. *Nature*, *458*(7242), 1158–1162. https://doi.org/10.1038/nature08017

Meinshausen, M., Vogel, E., Nauels, A., Lorbacher, K., Meinshausen, N., Etheridge, D. M., et al. (2017). Historical greenhouse gas concentrations for climate modelling (CMIP6). *Geoscientific Model Development*, *10*(5), 2057–2116. https://doi.org/10.5194/gmd-10-2057-2017

Murphy, D. M., Solomon, S., Portmann, R. W., Rosenlof, K. H., Forster, P. M., & Wong, T. (2009). An observationally based energy balance for the Earth since 1950. *Journal of Geophysical Research*, *114*(D17), D17107. https://doi.org/10.1029/2009JD012105

Myhre, G., Shindell, D., Bréon, F.-M., Collins, W., Fuglestvedt, J., Huang, J., et al. (2013). Anthropogenic and Natural Radiative Forcing. In Intergovernmental Panel on Climate Change (Ed.), *Climate Change 2013 - The Physical Science Basis* (pp. 659–740). Cambridge: Cambridge University Press. https://doi.org/10.1017/CBO9781107415324.018

Myhre, G., Samset, B. H., Schulz, M., Balkanski, Y., Bauer, S., Berntsen, T. K., et al. (2013). Radiative forcing of the direct aerosol effect from AeroCom Phase II simulations. *Atmospheric Chemistry and Physics*, *13*(4), 1853–1877. https://doi.org/10.5194/acp-13-1853-2013

Newman, P. A., Daniel, J. S., Waugh, D. W., & Nash, E. R. (2007). A new formulation of equivalent effective stratospheric chlorine (EESC). *Atmospheric Chemistry and Physics*, *7*(17), 4537–4552. https://doi.org/10.5194/acp-7-4537-2007

Nicholls, Z. R. J., Meinshausen, M., Lewis, J., Gieseke, R., Dommenget, D., Dorheim, K., et al. (2020). Reduced complexity model intercomparison project phase 1: Protocol, results and initial observations. *Geoscientific Model Development Discussions*, *2020*, 1–33. https://doi.org/10.5194/gmd-2019-375

Palmer, M. D. (2017). Reconciling Estimates of Ocean Heating and Earth's Radiation Budget. *Current Climate Change Reports*, *3*(1), 78–86. https://doi.org/10.1007/s40641-016-0053-7

Palmer, M. D., Harris, G. R., & Gregory, J. M. (2018). Extending CMIP5 projections of global mean temperature change and sea level rise due to thermal expansion using a physically-based emulator. *Environmental Research Letters*, *13*(8), 084003. https://doi.org/10.1088/1748-9326/aad2e4

Paulot, F., Paynter, D., Ginoux, P., Naik, V., & Horowitz, L. W. (2018). Changes in the aerosol direct radiative forcing from 2001 to 2015: observational constraints and regional mechanisms. *Atmospheric Chemistry and Physics*, *18*(17), 13265–13281. https://doi.org/10.5194/acp-18-13265-2018

Pincus, R., Forster, P. M., & Stevens, B. (2016). The Radiative Forcing Model Intercomparison Project (RFMIP): experimental protocol for CMIP6. *Geoscientific Model Development*, *9*(9), 3447–3460. https://doi.org/10.5194/gmd-9-3447-2016

Rap, A., Scott, C. E., Spracklen, D. V, Bellouin, N., Forster, P. M., Carslaw, K. S., et al. (2013). Natural aerosol direct and indirect radiative effects. *Geophysical Research Letters*, *40*(12), 3297–3301. https://doi.org/10.1002/grl.50441

Regayre, L. A., Pringle, K. J., Booth, B. B. B., Lee, L. A., Mann, G. W., Browse, J., et al. (2014). Uncertainty in the magnitude of aerosol-cloud radiative forcing over recent decades. *Geophysical Research Letters*, *41*(24), 9040–9049. https://doi.org/10.1002/2014GL062029

Richardson, M., Cowtan, K., Hawkins, E., & Stolpe, M. B. (2016). Reconciled climate response estimates from climate models and the energy budget of Earth. *Nature Climate Change*, *6*(10), 931–935. https://doi.org/10.1038/nclimate3066

Rogelj, J., Forster, P. M., Kriegler, E., Smith, C. J., & Séférian, R. (2019). Estimating and tracking the remaining carbon budget for stringent climate targets. *Nature*, *571*(7765), 335–342. https://doi.org/10.1038/s41586-019-1368-z

Rugenstein, M., Bloch-Johnson, J., Gregory, J., Andrews, T., Mauritsen, T., Li, C., et al. (2020). Equilibrium Climate Sensitivity Estimated by Equilibrating Climate Models. *Geophysical Research Letters*, *47*(4), e2019GL083898. https://doi.org/10.1029/2019GL083898

von Schuckmann, K., Cheng, L., Palmer, M. D., Tassone, C., Aich, V., Adusumilli, S., et al. (2020). Heat stored in the Earth system: Where does the energy go? The GCOS Earth heat inventory team. *Earth System Science Data Discussions*, *2020*, 1–45. https://doi.org/10.5194/essd-2019-255

Seland, Ø., Bentsen, M., Seland Graff, L., Olivié, D., Toniazzo, T., Gjermundsen, A., et al. (2020). The Norwegian Earth System Model, NorESM2 -- Evaluation of theCMIP6 DECK and historical simulations. *Geoscientific Model Development Discussions*, *2020*, 1–68. https://doi.org/10.5194/gmd-2019-378

Sellar, A. A., Jones, C. G., Mulcahy, J. P., Tang, Y., Yool, A., Wiltshire, A., et al. (2019).

UKESM1: Description and Evaluation of the U.K. Earth System Model. *Journal of Advances in Modeling Earth Systems*, *11*(12), 4513–4558. https://doi.org/10.1029/2019MS001739

Sherwood, S., Webb, M. J., Annan, J. D., Armour, K. C., Forster, P. M., Hargreaves, J. C., et al. (2020). An assessment of Earth's climate sensitivity using multiple lines of evidence. *Reviews of Geophysics*, *n/a*(n/a), e2019RG000678. https://doi.org/10.1029/2019RG000678

Skeie, R. B., Berntsen, T., Aldrin, M., Holden, M., & Myhre, G. (2018). Climate sensitivity estimates – sensitivity to radiative forcing time series and observational data. *Earth System Dynamics*, *9*(2), 879–894. https://doi.org/10.5194/esd-9-879-2018

Smith, C. J., Forster, P. M., Allen, M., Leach, N., Millar, R. J., Passerello, G. A., & Regayre, L. A. (2018). FAIR v1.3: a simple emissions-based impulse response and carbon cycle model. *Geoscientific Model Development*, *11*(6), 2273–2297. https://doi.org/10.5194/gmd-11-2273-2018

Smith, C. J., Kramer, R. J., Myhre, G., Forster, P. M., Soden, B. J., Andrews, T., et al. (2018). Understanding Rapid Adjustments to Diverse Forcing Agents. *Geophysical Research Letters*, *45*(21), 12,023-12,031. https://doi.org/10.1029/2018GL079826

Smith, C. J., Kramer, R. J., Myhre, G., Alterskjær, K., Collins, W., Sima, A., et al. (2020). Effective radiative forcing and adjustments in CMIP6 models. *Atmospheric Chemistry and Physics Discussions*, *2020*, 1–37. https://doi.org/10.5194/acp-2019-1212

Stevens, B. (2015). Rethinking the Lower Bound on Aerosol Radiative Forcing. *Journal of Climate*, *28*(12), 4794–4819. https://doi.org/10.1175/JCLI-D-14-00656.1

Stevenson, D. S., Young, P. J., Naik, V., Lamarque, J.-F., Shindell, D. T., Voulgarakis, A., et al. (2013). Tropospheric ozone changes, radiative forcing and attribution to emissions in the Atmospheric Chemistry and Climate Model Intercomparison Project (ACCMIP). *Atmospheric Chemistry and Physics*, *13*(6), 3063–3085. https://doi.org/10.5194/acp-13-3063-2013

Stohl, A., Aamaas, B., Amann, M., Baker, L. H., Bellouin, N., Berntsen, T. K., et al. (2015). Evaluating the climate and air quality impacts of short-lived pollutants. *Atmospheric Chemistry and Physics*, *15*(18), 10529–10566. https://doi.org/10.5194/acp-15-10529-2015

Swart, N. C., Cole, J. N. S., Kharin, V. V, Lazare, M., Scinocca, J. F., Gillett, N. P., et al. (2019). The Canadian Earth System Model version 5 (CanESM5.0.3). *Geoscientific Model Development*, *12*(11), 4823–4873. https://doi.org/10.5194/gmd-12-4823-2019

Tanaka, K., & Raddatz, T. (2011). Correlation between climate sensitivity and aerosol forcing and its implication for the "climate trap." *Climatic Change*, *109*(3–4), 815–825. https://doi.org/10.1007/s10584-011-0323-2

Tatebe, H., Ogura, T., Nitta, T., Komuro, Y., Ogochi, K., Takemura, T., et al. (2019). Description and basic evaluation of simulated mean state, internal variability, and climate sensitivity in MIROC6. *Geoscientific Model Development*, *12*(7), 2727–2765. https://doi.org/10.5194/gmd-12-2727-2019

Taylor, K. E., Crucifix, M., Braconnot, P., Hewitt, C. D., Doutriaux, C., Broccoli, A. J., et al. (2007). Estimating Shortwave Radiative Forcing and Response in Climate Models. *Journal*

878 *of Climate*, *20*(11), 2530–2543. https://doi.org/10.1175/JCLI4143.1

879 Thornhill, G. D., Collins, W. J., Kramer, R. J., Olivié, D., O'Connor, F., Abraham, N. L., et al.
880 (2020). Effective Radiative forcing from emissions of reactive gases and aerosols -- a
881 multimodel comparison. *Atmospheric Chemistry and Physics Discussions*, *2020*, 1–29.
882 https://doi.org/10.5194/acp-2019-1205

883 Toohey, M., & Sigl, M. (2017). Volcanic stratospheric sulfur injections and aerosol optical depth
884 from 500 BCE to 1900 CE. *Earth System Science Data*, *9*(2), 809–831.
885 https://doi.org/10.5194/essd-9-809-2017

886 Vieira, L. E. A., Solanki, S. K., Krivova, N. A., & Usoskin, I. (2011). Evolution of the solar
887 irradiance during the Holocene. *Astronomy & Astrophysics*, *531*, A6.
888 https://doi.org/10.1051/0004-6361/201015843

889 Wilcox, L. J., Highwood, E. J., Booth, B. B. B., & Carslaw, K. S. (2015). Quantifying sources of
890 inter-model diversity in the cloud albedo effect. *Geophysical Research Letters*, *42*(5), 1568–
891 1575. https://doi.org/10.1002/2015GL063301

892 Williams, K. D., Copsey, D., Blockley, E. W., Bodas-Salcedo, A., Calvert, D., Comer, R., et al.
893 (2018). The Met Office Global Coupled Model 3.0 and 3.1 (GC3.0 and GC3.1)
894 Configurations. *Journal of Advances in Modeling Earth Systems*, *10*(2), 357–380.
895 https://doi.org/10.1002/2017MS001115

896 Zelinka, M. D., Andrews, T., Forster, P. M., & Taylor, K. E. (2014). Quantifying components of
897 aerosol-cloud-radiation interactions in climate models. *Journal of Geophysical Research:*
898 *Atmospheres*, *119*(12), 7599–7615. https://doi.org/10.1002/2014JD021710

899 Zheng, B., Tong, D., Li, M., Liu, F., Hong, C., Geng, G., et al. (2018). Trends in China's
900 anthropogenic emissions since 2010 as the consequence of clean air actions. *Atmospheric*
901 *Chemistry and Physics*, *18*(19), 14095–14111. https://doi.org/10.5194/acp-18-14095-2018

902